INTERNATIONAL JOURNAL OF
NUMERICAL ANALYSIS AND MODELING
Volume 7, Number 2, Pages 373–391

EFFICIENT PARALLEL HYBRID COMPUTATIONS FOR THREE-DIMENSIONAL WAVE EQUATION PRESTACK DEPTH IMAGING

WENSHENG ZHANG AND YAU-SHU WONG

Abstract. Three-dimensional wave equation prestack depth imaging is an important tool in reconstructing images of complex subsurface structures, and it has become a technique gaining wide popularity in oil and gas industry. This is a large-scale scientific computing problem and can be considered a process of data continuation downward with the surface data or the boundary data, such as the shot-gather data. In this paper, we first discuss the decomposition of a two-way wave equation and investigate four different approaches to approximate the square-root operator. Using the known shot-gather data as input, an unconditional stable hybrid method for the wavefield extrapolation is presented. The most attractive feature of the proposed method is that it has a natural parallel characteristic and can be effectively implemented using a cluster of PCs, in which each processor performs its own shot-gather imaging independently. To demonstrate the computational efficiency and the power of the parallel hybrid algorithm, we present two case studies: one is the well-known SEG/EAEG subsalt model which has been commonly used for validation of the prestack depth imaging algorithms, and the other is the application to a 3D wavefield extrapolation problem with real data provided by the China National Petroleum Corporation. The results clearly show the capability of the proposed method, and it demonstrates that the algorithm can be effectively implemented as a practical engineering tool for 3D prestack depth imaging.

Key Words. prestack depth imaging, prestack migration, wavefield extrapolation, wave equation, hybrid method, parallel compuation, MPI

1. Introduction

The three-dimensional prestack depth migration or imaging is an important and effective engineering tool widely used in oil and gas industry, and it has become a standard technique for complex geological structures exploration. The 3D imaging process can be regarded as a data continuation downward with the surface data such as the shot-gather data. The downward continuation of the prestack data should be carried out in the 5D-space of a full 3D prestack geometry (recording time, source surface location, and receiver surface location). Due to the tremendous amount of the raw or field data, this requires a very expensive computational cost. For obvious reasons, it is important to develop efficient methods which can be economically applied in exploration.

Received by the editors October 30, 2008 and, in revised form, October 16, 2009.

This research was supported by the National Key Foundation Project (No.10431030), the Chair Foundation of ICMSEC in 2008, and in part by the Natural Sciences and Engineering Research Council of Canada.

Generally speaking, there are two classes of methods: Kirchhoff and non Kirchhoff. The Kirchhoff approach proposed by Schneider (1978) is the most commonly used method for the prestack depth migration due to its high efficiency and great flexibility in dealing with 3D data geometry. It can be employed to efficiently migrate data sets with uneven spatial sampling and data sets that are subsets of the complete prestack data, such as common-offset cubes and common-azimuth cubes. These advantages have led the industry to adapt almost exclusively the Kirchhoff method for 3D prestack migration. It should be noted that the migration accuracy of the Kirchhoff approach relies on the high-frequency asymptotic ray approximation. In order to increase the imaging accuracy, more accurate ray-tracing scheme is required; however, the requirements of the multi-pathing and the correct amplitudes of each arrival are computationally expensive. For non-Kirchhoff methods, most of the computing resource is consumed in the calculation of the propagating wavefield components that are either equal to zero or they do not contribute to the final image. The performance of the non-Kirchhoff methods can be improved by developing fast algorithms such as the fast Fourier transform (FFT) and the use of parallel computations.

The inverse time migration (Baysal, et al., 1983) is one of the non-Kirchhoff migration methods. The technique is capable of obtaining wave solutions and is developed based on the full or a two-way wave equation. All reflections, including the multiples and arbitrary steep reflectors can be imaged, but the imaging precision is inferior to that of a one-way wave equation for complex velocity media and structures. In this paper, we focus on a one-way wave equation.

Unlike an asymptotic solution using a high-frequency assumption in the Kirchhoff migration, the methods based on a one-way wave extrapolation are derived from the full wave equation. Thus, it can handle large lateral velocity variations and steep dipping events. Various numerical algorithms have been implemented using this approach, for examples, the phase-shift method (Gazdag, 1978), the phase-shift plus interpolation method (Gazdag and Sguazzero, 1984), the split-step method (Stoffa, 1990) and the Fourier finite-difference method (Ristow and Rühl, 1995). These methods were originally developed for two spatial dimensional cases, but they are now extended to 3D applications for prestack depth migration.

By taking advantage of the fast Fourier transform Methods, Stolt (1978) implemented an efficient algorithm in the frequency-wavenumber domain, which is capable of dealing with the steep dips up to 90°; however, it can not handle the lateral velocity variations. To improve the Stolt's method, the phase-shift method which can adapt the media with velocity varying only in depth and the split-step Fourier (SSF) migration which can handle the lateral migration dip are proposed. A further enhancement can be achieved by applying the SSF method with taking account the multiple reference velocities and incorporating the Fourier finite-difference (FFD) method to attain the accuracy under the situation with a strong velocity contrast. The FFD method can be regarded as a cascade of the SSF method and the finite-difference method for downward continuation in applications to large lateral velocity variations and high steep reflectors.

Another type of approximating wave equation method is the plane wave imaging or the slant stack migration. Here, the data are first stacked with the raw shot-gather data. Ottolini and Claerbout (1984) presented a migration method for common midpoint slant stack seismic data in a constant velocity media. The common midpoint data are processed as a plane wave section and the migration is performed on the individual common midpoint plane wave sections. However,

the plane wave migration differs from the conventional slant stack migration in the sense that the regulated illumination approach now controls the complexity of the incident wavefield at the target level. This in turn leads to a highly accurate image as reported by Rietveld and Berkhout (1994). Migration by summing over several shots data together and imaging with a single migration are another migration algorithms with the wavefield synthesizing method. Readers interested for more details should refer to the works by Louis et al. (2000) and Zhang (2004).

The double square-root equation provides an alternative way for developing a migration method in the midpoint-offset coordinates. In this approach, the wavefield extrapolation is carried out with a double-square root (DSR) rather than a single-square root (SSR). The DSR prestack migration equation can be employed for images with strong velocity variations by using a phase-shift plus interpolation or a split-step correction. Popovici (1996) proposed a simple split-step modification to the DSR prestack migration, which has proven to be a powerful migration algorithm capable of handling strong lateral velocity variations and producing a very good imaging for the benchmark Marmousi model. However, compared with the 3D SSR prestack depth migration, the DSR migration is not computationally efficient because numerous Fourier transforms is needed in the computations. Biondi and Palacharla (1997) considered a 3D common-azimuthal DSR migration to reduce the computing cost, and the saving is achieved due to the computations are performed in the original 4D-space instead of the usual 5D-space for the application of the conventional full 3D prestack downward-continuation operator. Obviously, the 3D common-azimuthal DSR prestack migration has the limitation of a narrow azimuth.

With the advent in parallel computations, wave equation migration approach is currently emerging as a standard and practical tool for wavefield extrapolation. In this paper, we present hybrid methods for 3D shot-gather prestack depth migration. The most attractive feature of the proposed algorithms is that the performance can be significantly enhanced by massive parallelism. The parallel implementation using the MPI library ensures the platform portability and the efficiency for the spatial decomposition. Numerical simulations for two case studies are reported, and the computational results clearly demonstrate the proposed parallel hybrid algorithms are successful and computationally efficient.

2. Wavefield extrapolation

2.1. Acoustic approximation. We first review the acoustic approximation and present the physical explanation by the use of the wave equation. For an elastic inhomogeneous media, the governing equation for the motion in continuum is

$$\rho \frac{\partial^2 u_i}{\partial t^2} = \sum_{j=1}^{3} \frac{\partial \sigma_{ji}}{\partial x_j}, \qquad i = 1, 2, 3, \tag{1}$$

where $\mathbf{u} = (u_1, u_2, u_3)$ is the displacement of the particle at $(x_1, x_2, x_3) = (x, y, z)$. Let t and σ_{ji} denote the time and the stress component, respectively, and let the positive z-axis pointing downward. For a linear isotropic elastic media and by applying the Hook's law, the stress-displacement relation is given by

$$\sigma_{ji} = \sigma_{ij} = \lambda \delta_{ij} \nabla \cdot \mathbf{u} + \mu \left(\frac{\partial u_i}{\partial x_j} + \frac{\partial u_j}{\partial x_i} \right), \quad i, j = 1, 2, 3, \tag{2}$$

where λ and μ are known as the Lam*é* moduli, and δ_{ij} is the Kronecker symbol. Making an acoustic approximation for an elastic media, i.e., set $\mu = 0$ or $\sigma_{ij} =$

$0(i \neq j)$, we obtain the following equation from Eqs. (1) and (2)

$$\rho \frac{\partial^2 \mathbf{u}}{\partial t^2} = -\nabla p, \tag{3}$$

where $p = -\lambda \nabla \cdot \mathbf{u}$ is the pressure. Suppose λ and ρ are invariant with time, then

$$\begin{array}{ll} \frac{\partial^2 p}{\partial t^2} & = -\lambda \nabla \cdot (\frac{\partial^2 \mathbf{u}}{\partial t^2}) = -\lambda \nabla \cdot (-\frac{1}{\rho} \nabla p) \\ & = \lambda [\frac{1}{\rho} \nabla \cdot \nabla p + \nabla \frac{1}{\rho} \nabla p] \\ & = \frac{\lambda}{\rho} \nabla^2 p + \lambda \nabla \frac{1}{\rho} \nabla p. \end{array} \tag{4}$$

That is,

$$\nabla^2 p - \frac{1}{v^2} \frac{\partial^2 p}{\partial t^2} = \nabla \ln \rho \nabla p, \tag{5}$$

where $v = \sqrt{\frac{\lambda}{\rho}}$. Eq. (4) is an acoustic wave equation describing the dilatational wave. It is noted that there exists shear wave and various transmitted waves in an elastic media. Migration/imaging based on the acoustic wave equation provides an approximation which is reasonable and has been widely used in seismic image processing. The justifications are given as follows. First, the exact source generates both the dilatational wave and the surface wave. The surface wave, however, propagates only near the earth surface while the object interface to be imaged are much more deeper. Secondly, various transmitted shear waves are produced only when the incidence angle of the dilatational wave is sufficiently large; however, the data collecting geometry in the field usually adopts a small offset which implies a small incidence angle. Consequently, the transmitted waves are very weak or may not even exist. Therefore, the use of an acoustic approximation is usually very effective. Moreover, the density ρ in Eq. (5) can be treated as a constant since it varies very smoothly with the spatial positions. Therefore, the approximated 3D acoustic wave equation for imaging is simplified to

$$\frac{1}{v^2} \frac{\partial^2 p}{\partial t^2} - \frac{\partial^2 p}{\partial x^2} - \frac{\partial^2 p}{\partial y^2} - \frac{\partial^2 p}{\partial z^2} = 0, \tag{6}$$

where x, y, z are the space variables, $p(t, x, y, z)$ is the acoustic pressure and $v(x, y, z)$ is the medium velocity.

2.2. Wavefield splitting. The migration or imaging is a process extrapolating the given data on the surface (boundary values) downward in depth. Instead of using a two-way wave equation given in Eq. (6), we decouple a second-order equation into a system of two first-order partial differential equations. Introducing the Fourier transform of t, x and y for p and the function $f(t, x, y, z)$

$$f(\omega, k_x, k_y, z) = \frac{1}{(2\pi)^3} \int \int \int e^{i(\omega t - k_x x - k_y y)} f(t, x, y, z) dx dy dt, \tag{7}$$

where k_x and k_y are the wavenumbers, and ω is the angular frequency. Taking the Fourier transform of t, we get

$$\frac{\omega^2}{v^2} P + \frac{\partial^2 P}{\partial x^2} + \frac{\partial^2 P}{\partial y^2} + \frac{\partial^2 P}{\partial z^2} = 0, \tag{8}$$

where $P = P(\omega, x, y, z)$. It should be noted that while $P(\omega, x, y, 0)$ is known, $\frac{\partial P}{\partial z}|_{z=0}$ is unknown. It is difficult to employ the wavefield extrapolation using Eq.(8), since

two boundary conditions are required. The difficulty can be overcome by rewriting Eq. (8) as

$$\frac{\partial}{\partial z}\begin{bmatrix} P \\ \frac{\partial P}{\partial z} \end{bmatrix} = \begin{bmatrix} 0 & 1 \\ -(\frac{\omega^2}{v^2}+\frac{\partial^2}{\partial x^2}+\frac{\partial^2}{\partial y^2}) & 0 \end{bmatrix}\begin{bmatrix} P \\ \frac{\partial P}{\partial z} \end{bmatrix} := A\begin{bmatrix} P \\ \frac{\partial P}{\partial z} \end{bmatrix}. \tag{9}$$

The matrix A is then decomposed as

$$A = L\Lambda L^{-1}, \tag{10}$$

where

$$L = \begin{bmatrix} 1 & 1 \\ -i\sqrt{\frac{\omega^2}{v^2}+\frac{\partial^2}{\partial x^2}+\frac{\partial^2}{\partial y^2}} & i\sqrt{\frac{\omega^2}{v^2}+\frac{\partial^2}{\partial x^2}+\frac{\partial^2}{\partial y^2}} \end{bmatrix}, \tag{11}$$

$$\Lambda = \begin{bmatrix} -i\sqrt{\frac{\omega^2}{v^2}+\frac{\partial^2}{\partial x^2}+\frac{\partial^2}{\partial y^2}} & 0 \\ 0 & i\sqrt{\frac{\omega^2}{v^2}+\frac{\partial^2}{\partial x^2}+\frac{\partial^2}{\partial y^2}} \end{bmatrix}, \tag{12}$$

$$L^{-1} = \frac{1}{2}\begin{bmatrix} 1 & \frac{i}{\sqrt{\frac{\omega^2}{v^2}+\frac{\partial^2}{\partial x^2}+\frac{\partial^2}{\partial y^2}}} \\ 1 & -\frac{i}{\sqrt{\frac{\omega^2}{v^2}+\frac{\partial^2}{\partial x^2}+\frac{\partial^2}{\partial y^2}}} \end{bmatrix}. \tag{13}$$

Now, by taking the Fourier transforms for the three variables x, y, t in Eq. (6), we obtain the following equations in the frequency-wavenumber domain

$$(\frac{\partial^2}{\partial z^2}+k_z^2)P = (\frac{\partial}{\partial z}+ik_z)(\frac{\partial}{\partial z}-ik_z)P = 0, \tag{14}$$

where

$$k_z = \frac{\omega}{v}\sqrt{1-\frac{v^2}{\omega^2}(k_x^2+k_y^2)}, \tag{15}$$

is the square-root operator. The counterpart of the square-root operator in the frequency-space domain is given by

$$K_z = \frac{\omega}{v}\sqrt{1+\frac{v^2}{\omega^2}(\frac{\partial^2}{\partial x^2}+\frac{\partial^2}{\partial y^2})}. \tag{16}$$

Suppose the total wavefield P is decomposed into the downgoing wave D and the upcoming wave U. Then, D and U satisfy

$$P = D + U, \tag{17}$$

and

$$\frac{\partial P}{\partial z} = -i\sqrt{\frac{\omega^2}{v^2}+\frac{\partial^2}{\partial x^2}+\frac{\partial^2}{\partial y^2}}(D-U), \tag{18}$$

or expressed in a matrix notation

$$\begin{bmatrix} P \\ \frac{\partial P}{\partial z} \end{bmatrix} = L\begin{bmatrix} D \\ U \end{bmatrix}. \tag{19}$$

Hence, Eq. (9) can be rewritten as

$$\frac{\partial}{\partial z}L\begin{bmatrix} D \\ U \end{bmatrix} = (L\Lambda L^{-1})L\begin{bmatrix} D \\ U \end{bmatrix}. \tag{20}$$

or

$$\frac{\partial}{\partial z}\begin{bmatrix} D \\ U \end{bmatrix} = (\Lambda - L^{-1}\frac{\partial L}{\partial z})\begin{bmatrix} D \\ U \end{bmatrix}. \tag{21}$$

That is,

$$\frac{\partial D}{\partial z} = -i\sqrt{\frac{\omega^2}{v^2} + \frac{\partial^2}{\partial x^2} + \frac{\partial^2}{\partial y^2}}D - \frac{1}{2k_z}\frac{\partial k_z}{\partial z}(D - U), \tag{22}$$

$$\frac{\partial U}{\partial z} = i\sqrt{\frac{\omega^2}{v^2} + \frac{\partial^2}{\partial x^2} + \frac{\partial^2}{\partial y^2}}U + \frac{1}{2k_z}\frac{\partial k_z}{\partial z}(D - U). \tag{23}$$

Eqs. (22) and (23) represent accurate one-way wave equations for the wavefield extrapolation in an inhomogeneous media. Similarly, the extrapolation for a two-way wave equation can be implemented using the above two equations; however, the downgoing wavefield D and the upcoming wavefield U are coupled in Eqs. (22) and (23). The downgoing wavefield is needed when one extrapolates the upcoming wavefield in depth with Eq. (23), while the upcoming wavefield is required when extrapolating the downgoing wavefield using Eq. (22). Consequently, the extrapolation process is quite complicated. However, if D is the incident wave with an incidence angle below the critical angle, then the reflected wavefield is small compared to D. On the contrary, if U is the incident wave with an incidence angle below the critical angle, the reflected wavefield will also be a small quantity. Hence, by neglecting the critical angle, Eqs. (22) and (23) can be simplified as

$$\frac{\partial D}{\partial z} = -i\sqrt{\frac{\omega^2}{v^2} + \frac{\partial^2}{\partial x^2} + \frac{\partial^2}{\partial y^2}}D - \frac{1}{2k_z}\frac{\partial k_z}{\partial z}D, \tag{24}$$

$$\frac{\partial U}{\partial z} = i\sqrt{\frac{\omega^2}{v^2} + \frac{\partial^2}{\partial x^2} + \frac{\partial^2}{\partial y^2}}U + \frac{1}{2k_z}\frac{\partial k_z}{\partial z}(-U). \tag{25}$$

Eqs. (24) and (25) are decoupled one-way wave equations for the downgoing and the upcoimg wavefield, respectively. If the media is homogeneous along the z-coordinate (it may be inhomogeneous in lateral directions), then $\frac{\partial K_z}{\partial z} = 0$ and Eqs. (24) and (25) can be reduced to

$$\frac{\partial D}{\partial z} = -i\sqrt{\frac{\omega^2}{v^2} + \frac{\partial^2}{\partial x^2} + \frac{\partial^2}{\partial y^2}}D, \tag{26}$$

$$\frac{\partial U}{\partial z} = i\sqrt{\frac{\omega^2}{v^2} + \frac{\partial^2}{\partial x^2} + \frac{\partial^2}{\partial y^2}}U. \tag{27}$$

Generally speaking, we assume that the media is homogeneous in the vertical z-direction with an extrapolating depth step $[z, z + \Delta z]$. Hence, using one boundary value, we can solve Eqs. (26) and (27), and this is also valid approximately for the inhomogeneous cases.

In the frequency and wavenumber domain, the downgoing wave Eq. (26) becomes

$$\frac{\partial D}{\partial z} = -ik_z D = -i\frac{\omega}{v}\sqrt{1 - \frac{v^2}{\omega^2}(k_x^2 + k_y^2)}D, \tag{28}$$

and the upcoming wave Eq. (27) can be expressed as

$$\frac{\partial U}{\partial z} = +ik_z U = +i\frac{\omega}{v}\sqrt{1 - \frac{v^2}{\omega^2}(k_x^2 + k_y^2)}U, \tag{29}$$

respectively.

2.3. Approximating the square-root operator. From a computational point of view, the major difficulty in dealing with Eqs. (28) or (29) is that they are non-local pseudo-differential equations. The key step in resolving the problem is to approximate the square-root operator. One notes that if θ is the incidence angle of planewave and ϕ is the azimuthal angle of plenewave, then $\frac{vk_x}{\omega} = \sin\theta\cos\phi$ and $\frac{vk_y}{\omega} = \sin\theta\sin\phi$. In the following, we discuss four possible ways for approximating the square-root operator k_z. Let define

$$k_z = \frac{\omega}{v}\bar{k}_z, \quad \bar{k}_z = \sqrt{1 - \frac{v^2}{\omega^2}(k_x^2 + k_y^2)}. \tag{30}$$

1. In the first approach, we apply the general Padé approximation. By making the orthogonalization for the functions 1, t, t^2 in $[0,1]$ with the weight $\omega(t) = 1+t$. The orthogonal polynomial can be written as

$$Q_n(t) = (t - a_n)Q_{n-1}(t) - b_n Q_{n-2}(t), \tag{31}$$

where

$$Q_0(t) = 1, \quad Q_1(t) = t - a_1, \quad a_n = \frac{(tQ_{n-1}, Q_{n-1})}{(Q_{n-1}, Q_{n-1})}, \quad b_n = \frac{(tQ_{n-1}, Q_{n-2})}{(Q_{n-2}, Q_{n-2})}. \tag{32}$$

Then, we obtain the following approximation expression

$$\sqrt{1-t^2} = \frac{p_0 Q_0(t) + p_1 Q_1(t)}{Q_0(t) + q_1 Q_1(t)} := \frac{a_0 - a_1 t}{b_0 - b_1 t}, \tag{33}$$

where

$$a_0 = 2.020, \quad a_1 = 2.081, \quad b_0 = 1.998, \quad b_1 = 1.752. \tag{34}$$

These coefficients are determined by requiring

$$(\bar{k}_z(t) - \frac{p_0 Q_0(t) + p_1 Q_1(t)}{q_0 Q_0(t) + q_1 Q_1(t)}, Q_i(t)) = 0, \quad i = 0, 1, 2. \tag{35}$$

Setting

$$t_1 = \frac{v}{\omega}k_x, \quad t_2 = \frac{v}{\omega}k_y, \quad t^2 = \frac{v^2}{\omega^2}(k_x^2 + k_y^2), \tag{36}$$

then $\bar{k}_z$ can be approximated by

$$\begin{aligned}
\bar{k}_z = \sqrt{1-t^2} &= \sqrt{1 - t_1^2 - t_2^2} = 1 - \frac{1}{2}t_1^2 - \frac{1}{2}t_2^2 + O(t^4) \\
&= (1 - \frac{1}{2}t_1^2) + (1 - \frac{1}{2}t_2^2) - 1 + O(t^4) \\
&= \sqrt{1 - t_1^2} + \sqrt{1 - t_2^2} - 1 + O(t^4) \\
&= \frac{a_0 - a_1 t_1}{b_0 - b_1 t_1} + \frac{a_0 - a_1 t_2}{b_0 - b_1 t_2} - 1 + O(t^4) \\
&\approx \frac{a_0 - a_1 t_1}{b_0 - b_1 t_1} + \frac{a_0 - a_1 t_2}{b_0 - b_1 t_2} - 1. \qquad (37)
\end{aligned}$$

Here, the error term $O(t^4)$ is omitted. Therefore, k_z can be approximated by

$$k_z = \frac{\omega}{v}\Big[\frac{a_0 - a_1\frac{v}{\omega}k_x}{b_0 - b_1\frac{v}{\omega}k_x} + \frac{a_0 - a_1\frac{v}{\omega}k_y}{b_0 - b_1\frac{v}{\omega}k_y} - 1\Big]. \tag{38}$$

2. In the second method, the approximation is based on the Чебыщев expression

$$\bar{k}_z(t) = \sqrt{1-t} = \sum_{k=0}^{\infty} C_k T_k(t), \quad t = \frac{v^2}{\omega^2}(k_x^2 + k_y^2) := \sin^2\theta. \tag{39}$$

Hence, $\bar{k}_z(t)$ is approximated by using the following rational expression

$$R_{mn}(t) = \frac{p_m(t)}{q_n(t)} \tag{40}$$

where

$$p_m(t) = \sum_{i=0}^{m} a_i T_i(t), \qquad q_n(t) = \sum_{j=0}^{n} b_j T_j(t). \tag{41}$$

The coefficients $a_i (i = 0, 1, \cdots, m)$ and $b_j (j = 0, 1, \cdots, n)$ are the non-zero solutions of the following system, and setting $b_0 = 1$:

$$\begin{aligned} a_0 &= b_0 C_0 + \tfrac{1}{2} \sum_{r=1}^{n} b_r C_r, \\ a_k &= b_0 C_k + \tfrac{1}{2} b_k C_0 + \tfrac{1}{2} \sum_{r=1}^{n} b_r (C_{r+k} + C_{|r-k|}), \quad k = 1, 2, \cdots, m+n. \end{aligned} \tag{42}$$

The following expression is then used to approximate $\bar{k}(t)$ in (39)

$$\bar{k}(t) = \frac{1}{4} A_0 + \sum_{k=1}^{N-1} A_k T_k(t) + \frac{1}{4} A_N T_N(t), \tag{43}$$

where

$$A_k = \frac{2}{N} \sum_{j=0}^{N} f(\cos \frac{j\pi}{N}) \cos \frac{j\pi k}{N}, \quad k = 0, 1, \cdots, N. \tag{44}$$

If we let $m = n = 1$ in Eq. (41) and set $N = 5$ in Eq. (43), we obtain the expression

$$\sqrt{1 - \sin^2 \theta} = 1 - \frac{0.4767 \sin^2 \theta}{1 - 0.3767 \sin^2 \theta}. \tag{45}$$

Thus the square-root operator can be approximated by

$$k_z \approx \frac{\omega}{v} [1 - \frac{0.4761 \frac{v^2}{\omega^2} (k_x^2 + k_y^2)}{1 - 0.3767 \frac{v^2}{\omega^2} (k_x^2 + k_y^2)}]. \tag{46}$$

3. Another possible approximation is to consider a Taylor expansion:

$$\sqrt{1 - t^2} \approx [1 - \frac{1}{2} t^2 - \frac{1}{8} t^4 - \cdots]. \tag{47}$$

Hence, it gives

$$k_z \approx \frac{\omega}{v} [1 - \frac{v^2}{2\omega^2} (k_x^2 + k_y^2) - \frac{v^4}{8\omega^4} (k_x^2 + k_y^2)^2 - \cdots]. \tag{48}$$

The approximation includes up to the fourth-order terms for the spatial derivatives. For practical computations, it is sufficed to use the first two terms to approximate k_z.

4. The fourth approximation for the square-root operator is developed from the continued fraction expansion of $\sqrt{1 - t^2}$:

$$S_{n+1} = 1 - \frac{t^2}{1 + S_n}, \quad S_0 = 1. \tag{49}$$

Hence, we get

$$\bar{k}_{z,n+1} = [1 - \frac{\frac{\omega^2}{v^2} (k_x^2 + k_y^2)}{1 + \bar{k}_{z,n}}], \quad \bar{k}_{z,0} = 1, \tag{50}$$

and the second-order approximation of k_z is given by

$$\bar{k}_{z,2} = \frac{\omega}{v}[1 - \frac{0.5\frac{\omega^2}{v^2}(k_x^2 + k_y^2)}{1 - 0.25\frac{\omega^2}{v^2}(k_x^2 + k_y^2)}]. \tag{51}$$

It should be noted that the approximation based on a second-order continued fraction expansion is as accurate as that using the fourth-order Taylor expansion, but it includes only the second-order terms for the spatial derivatives.

We now investigate the effectiveness of the four approximations (1, 2, 3 and 4) presented in this section. In Fig. 1, we compare the performance of the approximations with the exact value of the square-root operator. Here, we keep the first two terms in the Taylor expansion (47) for method 3, and the second-order continued fraction approximation is used for method 4. The test case is constructed by setting $t = \sin\theta$ in $\sqrt{1-t^2}$, and the x axis denotes the degree representing the dip of a reflector in the wave equation imaging process. The results show that method 2, namely the Чебыщев approximation, provides the best approximation. Among the four approximations, method 4 based on the second-order continued fraction expansion is less accurate compared to method 2, but is better than methods 1 and 3. Fig. 2 displays the absolute errors of the four approximations, in which the horizontal solid line corresponds to 1% error. It is of interest to note that the maximal angle of the four approximations crossing the 1% error threshold occurs at 33°, 65°, 31° and 48°, for methods 1, 2, 3 and 4, respectively. Obviously, the larger the value of the angle before reaching the 1% error threshold, the better the approximation for the square-root operator. Therefore, we conclude that method 2 using the Чебыщев expression gives the best approximation, and has a small error up to the 65° imaging dip.

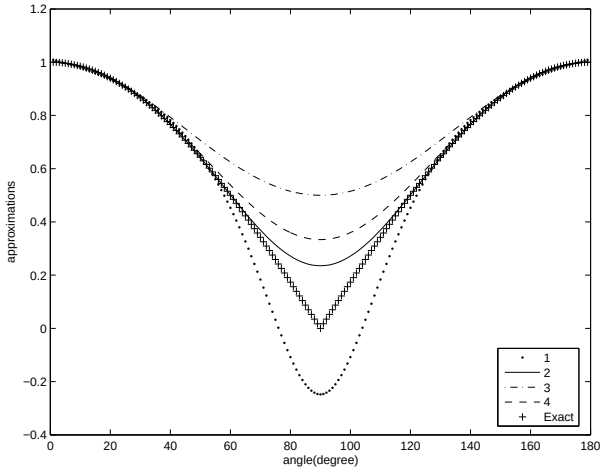

Figure 1. Comparisons of four approximations with exact value

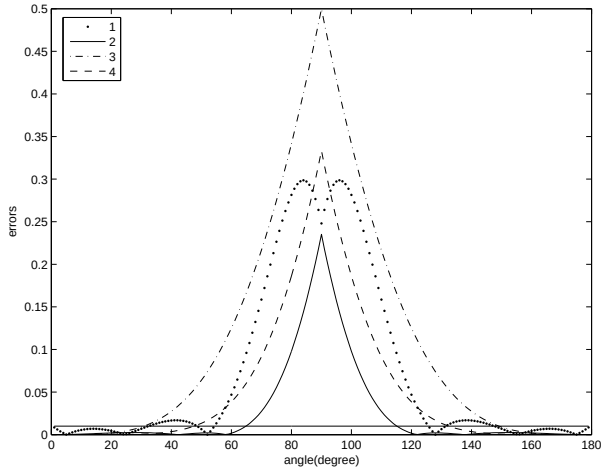

Figure 2. Absolute errors of four approximations, solid line corresponds to 1% error threshold

Based on the results illustrate in Figs. 1 and 2, we now present a general hybrid scheme. Using the identity formulae

$$\sqrt{1-t^2} = 1 - \frac{1}{\pi}\int_{-1}^{1} \sqrt{1-S^2}\frac{t^2}{1-t^2S^2}dS, \tag{52}$$

the square-root operator k_z can be rewritten as

$$k_z = \frac{\omega}{v}[1 - \frac{1}{\pi}\int_{-1}^{1} \sqrt{1-S^2}\frac{(vk_x)^2+(vk_y)^2}{\omega^2-(Svk_x)^2-(Svk_y)^2}]dS. \tag{53}$$

Then, by the use of the Gauss integral formulae

$$\frac{1}{\pi}\int_{0}^{1} \sqrt{1-S^2}f(S)dS \approx \frac{1}{2}\sum_{l=1}^{m} C_{m,l}f(S_{m,l}), \tag{54}$$

where

$$S_{m,l} = \cos(\frac{l\pi}{m+1}), \quad C_{m,l} = \frac{l}{m+1}\sin^2(\frac{l\pi}{m+1}). \tag{55}$$

Taking $m = 1$, $S_{1,1} = 0$, $C_{1,1} = 1$, inserting the expressions (53)$\sim$(55) into Eqs.(28) and (29), we obtain the 15° one-way wave equation. Letting $m = 2$, $S_{2,1} = -S_{2,2} = \frac{1}{2}$, $C_{2,1} = C_{2,2} = \frac{1}{2}$, it gives the 45° wave equation (Claerbout, 1985).

In order to include large lateral velocity variations, we introduce a reference velocity $v_0(z)$ which was also used in the reference of Ristow and Rühl (1995). The square-root operator k_z can now be approximated as

$$k_z \approx k_{z1} + k_{z2} + k_{z3}. \tag{56}$$

Therefore, the one-way wavefield extrapolation equation for the downgoing wave D and the upgoing wave U is given by

$$\frac{\partial P}{\partial z} = \pm i[k_{z1} + k_{z2} + k_{z3}]P, \tag{57}$$

where P represents D for the positive sign $+$ and U for the negative sign $-$, k_{z1}, k_{z2} and k_{z3} are defined as follows

$$k_{z1} = \sqrt{\frac{\omega^2}{v_0^2} - k_x^2 - k_y^2}, \quad k_{z2} = \frac{\omega}{v}(1 - \frac{v}{v_0}), \quad k_{z3} = \frac{b\frac{v}{\omega}(\frac{\partial^2}{\partial x^2} + \frac{\partial^2}{\partial y^2})}{1 + a\frac{v^2}{\omega^2}(\frac{\partial^2}{\partial x^2} + \frac{\partial^2}{\partial y^2})}. \tag{58}$$

The wavefield P downward continued at depth $z + \Delta z$ is computed from the wavefield at depth z using the formal expression

$$P(\omega, x, y, z + \Delta z) \approx P(\omega, x, y, z)e^{\pm i(k_{z1}+k_{z2}+k_{z3})\Delta z}. \tag{59}$$

Notice that k_{z1} is in the frequency-wavenumber domain, whereas k_{z2} and k_{z3} are in the frequency-space domain. The parameters a and b in k_{z3} are chosen to allow large migration angle in the one-way wave equation. Ristow and Dühl (1995) proposed $a = \frac{1}{2}(1 - \frac{v_0}{v})$ and $b = \frac{1}{4}[(\frac{v_0}{v})^2 + \frac{v_0}{v} + 1]$, and recently, Zhang and Zhang (2006) suggested $a = \frac{1}{2}(1 - \frac{v_0}{v})$ and $b = 0.3767[(\frac{v_0}{v})^2 + 1]$, in which the factor 0.3767 was due to the Чебыщев approximation. Detailed comparisons of the two selections for a and b are reported in Zhang and Zhang (2006). The wavefield extrapolation can now be carried out in the following three steps. The first step is the phase-shift correction in the frequency-wavenumber domain. The time-shift computation in the second step is in the frequency-space domain, and then follows by the third step - the finite-difference migration which is also in the frequency-space domain. Since the wavefield extrapolation is completed alternatively in the frequency-wavenumber and in the frequency-space domain, it is referred as the hybrid method.

2.4. Wavefield extrapolation algorithms. The first step of wavefield extrapolation can be formulated as

$$P_{k,l}^{n+1} = e^{\pm ik_{z1}\Delta z}P_{k,l}^n, \tag{60}$$

where $k = 0, \cdots, N_x - 1$; $l = 0, \cdots, N_y - 1$; $n = 0, \cdots, N_z - 1$, and the computations are completed in the frequency-wavenumber domain. The second step is expressed

$$P_{k,l}^{n+1} = e^{\pm ik_{z2}\Delta z}P_{k,l}^n, \tag{61}$$

which is computed in the frequency-space domain. We now present the detailed implementation for the third step. The one-way wave equation corresponding to the finite-difference migration operator k_{z3} is given by

$$\frac{\partial P}{\partial z} = \pm i\frac{b\frac{v}{\omega}(\frac{\partial^2}{\partial x^2} + \frac{\partial^2}{\partial y^2})}{1 + a\frac{v^2}{\omega^2}(\frac{\partial^2 x}{\partial x^2} + \frac{\partial^2}{\partial y^2})}P. \tag{62}$$

The equation takes account of the effects due to the wave diffraction. For simplicity, we choose the positive sign $+$ in Eq.(62), it then leads to the following alternating directional implicit (ADI) scheme

$$\begin{aligned} [1 + (\alpha_1 - i\beta_1)\delta_x^2]P_{k,l}^{n+1/2} &= [1 + (\alpha_1 + i\beta_1)\delta_x^2]P_{k,l}^n, \\ [1 + (\alpha_2 - i\beta_2)\delta_y^2]P_{k,l}^{n+1} &= [1 + (\alpha_2 + i\beta_2)\delta_y^2]P_{k,l}^{n+1/2}. \end{aligned} \tag{63}$$

Here, $P_{k,l}^n$ represents $P(\omega, k\Delta x, l\Delta y, n\Delta z)$, δ_x^2 and δ_y^2 are the second-order central differences with respect to x and y, respectively. The spatial steps in x, y and z are denoted by Δx, Δy and Δz, respectively. The coefficients α_1, α_2, β_1 and β_2 are defined as

$$\alpha_1 = \frac{av^2}{\omega^2\Delta x^2}, \quad \alpha_2 = \frac{av^2}{\omega^2\Delta y^2}, \quad \beta_1 = \frac{b\Delta z v}{2\omega\Delta x^2}, \quad \beta_2 = \frac{b\Delta z v}{2\omega\Delta y^2}. \tag{64}$$

The ADI scheme is computationally efficient, and only the solutions of the tri-diagonal matrices resulting from splitting in the $x-$ and $y-$ direction given in Eq. (63) are required. The ADI has the accuracy of $O(\Delta x^2+\Delta y^2+\Delta z^2)$. Even though the ADI scheme may cause numerical anisotropic errors, it is possible to reduce the azimuthal errors using the multi-way methods (Collina and Joly, 1995; Ristow and Rühl, 1997). Recently, Zhang and Zhang (2006) proposed an algorithm to the eliminate numerical anisotropic errors.

To analysis the stability of the ADI scheme, we apply the Fourier analysis method (Thomas, 1995). First, by eliminating the variable $P_{k,l}^{n+\frac{1}{2}}$, the ADI can be rewritten as

$$[1+(\alpha_1-i\beta_1)\delta_x^2][1+(\alpha_2-i\beta_2)\delta_y^2]P_{k,l}^{n+1} = [1+(\alpha_2+i\beta_2)\delta_y^2][1+(\alpha_1+i\beta_1)\delta_x^2]P_{k,l}^{n}. \tag{65}$$

Here, we suppose the operators δ_x^2 and δ_y^2 are interchangeable, which is usually satisfied for a rectangular domain. Note that the errors between the exact solutions and the numerical solutions, $\varepsilon_{k,l}^n$, also satisfy similar equation given in Eq. (65). We now consider a Fourier component of the computational error, which is given by

$$\varepsilon_{k,l}^n = V^n e^{i\sigma_1 k\Delta x} e^{i\sigma_2 l\Delta y}, \tag{66}$$

where $i=\sqrt{-1}$, σ_1 and σ_2 are the spatial wavenumbers in $x-$ and $y-$ direction, respectively, V^n is the Fourier amplitude at a particular time step n. Substituting Eq. (66) into Eq. (64), we obtain

$$\begin{array}{c}[1+(\alpha_1-i\beta_1)(-4\sin^2\frac{\alpha_1\Delta x}{2})+(\alpha_2-i\beta_2)(-4\sin^2\frac{\alpha_2\Delta y}{2})+\\ (\alpha_1-i\beta_1)(\alpha_2-i\beta_2)(-4\sin^2\frac{\alpha_1\Delta x}{2})(-4\sin^2\frac{\alpha_2\Delta y}{2})]V^{n+1}\\ =[1+(\alpha_1+i\beta_1)(-4\sin^2\frac{\alpha_1\Delta x}{2})+(\alpha_2+i\beta_2)(-4\sin^2\frac{\alpha_2\Delta y}{2})+\\ (\alpha_1+i\beta_1)(\alpha_2+i\beta_2)(-4\sin^2\frac{\alpha_1\Delta x}{2})(-4\sin^2\frac{\alpha_2\Delta y}{2})]V^{n}.\end{array} \tag{67}$$

Thus, the amplifying factor $G=\frac{V^{n+1}}{V^n}$ for the errors is given by

$$G=\frac{c+id}{c-id}, \tag{68}$$

where

$$\begin{aligned} c &= 1-4\alpha_1\sin^2\tfrac{\sigma_1\Delta x}{2}-4\alpha_2\sin^2\tfrac{\sigma_2\Delta y}{2}+16(\alpha_1\alpha_2-\beta_1\beta_2)\sin^2\tfrac{\sigma_1\Delta x}{2}\sin^2\tfrac{\sigma_2\Delta y}{2},\\ d &= -4\beta_1\sin^2\tfrac{\sigma_1\Delta x}{2}-4\beta_2\sin^2\tfrac{\sigma_2\Delta y}{2}+16(\alpha_1\beta_2+\alpha_2\beta_1)\sin^2\tfrac{\sigma_1\Delta x}{2}\sin^2\tfrac{\sigma_2\Delta y}{2}. \end{aligned} \tag{69}$$

In fact, G is the ratio of the error representing the Fourier amplitudes as a function of the time steps. Therefore, we require $|G|\le 1$ to ensure the stability, and it is unconditional stable when $|G|=1$. The ADI scheme considered in this paper is a two-step implicit scheme, and Hale (1999) presented stable explicit schemes for the wavefield extrapolation.

The hybrid algorithm for the wavefield extrapolation consists of the following steps:

Step 1. Apply the fast Fourier transform (FFT) with respect to t for the given shot-gather data $p(t,x,y,z)$, i.e.,

$$p_1(\omega,x,y,z)=\frac{1}{2\pi}\int p(t,x,y,z)e^{i\omega t}dt. \tag{70}$$

In discrete form, it is given by

$$p_1(l,x,y,z)\approx\frac{\Delta t}{2\pi}\sum_{k=0}^{N_t-1}p(k,x,y,z)e^{i\frac{2n\pi k}{N_t}},\quad l=0,1,\cdots,N_t-1, \tag{71}$$

where N_t is the sampling points in t.

Step 2. Apply FFT with respect to x and y for the data $p_1(\omega, x, y, z)$ at the extrapolation depth z, i.e,

$$FFT_{x,y}[p(\omega, x, y, z)] = \frac{1}{(2\pi)^2} \int\int p_1(\omega, x, y, z) e^{-i(k_x x + k_y y)} dxdy. \tag{72}$$

Suppose N_x and N_y are the period sampling points in $x-$ and $y-$ direction, respectively, the discrete version for Eq. (70) is

$$\begin{aligned} \tilde{p}(\omega, k, l, z) \approx \tfrac{\Delta x \Delta y}{(2\pi)^2} \sum_{m=0}^{N_x-1} \sum_{n=0}^{N_y-1} p_1(\omega, k, l, z) e^{-i(\frac{2\pi km}{N_x} + \frac{2\pi ln}{N_y})} \\ k = 0, 1, \cdots, N_x - 1; l = 0, 1, \cdots, N_y - 1. \end{aligned} \tag{73}$$

Step 3. Compute the phase-shift correction

$$P(\omega, k_x, k_y, z + \Delta z) = FFT_{x,y}[p_1(\omega, x, y, z)] e^{iA_1 \Delta z}. \tag{74}$$

Step 4. Transform the inverse FFT with respect to k_x and k_y for data $P(\omega, k_x, k_y, z + \Delta z)$, i.e., $IFFT_{k_k,k_y}[P(\omega, k_x, k_y, z + \Delta z)]$.

Step 5. Compute the time-shift correction

$$p_1(\omega, x, y, z + \Delta z) = e^{i\omega(\frac{1}{v} - \frac{1}{v_0})} IFFT_{k_k,k_y}[P(\omega, k_x, k_y, z + \Delta z)]. \tag{75}$$

Step 6. Perform the finite-difference computations with data $p_1(\omega, x, y, z + \Delta z)$ in the frequency-space domain using Eqs. (63) and (64). Then, return to Step 2 until the maximum depth is reached. To avoid the artifacts due to the complex wavenumebr, we filter the field in the domain where $k_x^2 + k_y^2 \geq \frac{\omega^2}{v^2}$ at each extrapolation.

2.5. Imaging and boundary conditions. The subsurface images are reconstructed by extrapolating the downgoing wavefield D and the upcoming wavefield U simultaneously. Now, applying the imaging condition proposed by Claerbout (1971)

$$I(\boldsymbol{x}) = \sum_{\boldsymbol{x}_s} \sum_{\omega} UD^* \tag{76}$$

at each image point, where $\boldsymbol{x} = (x, y, z)$ is the imaging position, ω is the angular frequency and $\boldsymbol{x}_s = (x_s, y_s, z_s)$ is the location for the source. $U(\omega, \boldsymbol{x}; \boldsymbol{x}_s)$ and $D(\omega, \boldsymbol{x}; \boldsymbol{x}_s)$ are the upgoing/receiver and the downgoing/source wavefields at $\boldsymbol{x}_s$, respectively. D^* denotes the complex conjugate of D. The reflection coefficient R can be written as

$$R(\boldsymbol{x}) = \sum_{\boldsymbol{x}_s} \sum_{\omega} \frac{UD^*}{\varepsilon + DD^*}. \tag{77}$$

A small positive number ε is added to the denominator to improve the stability. The imaging condition Eq. (77) reveals the reflectivity variations of the interface. However, it usually produces additional noises to the resulting images as ε is related to the ratio of the single/noise. Finally, the entire images Ω are obtained by summing the partial images of different shot lines:

$$\Omega(\boldsymbol{x}) = \sum_{\boldsymbol{x}_l} I(\boldsymbol{x}) \delta(\boldsymbol{x}_s - \boldsymbol{x}_l), \tag{78}$$

where $\boldsymbol{x}_l = (x_l, y_l, z_l)$ is the shot-line position.

In order to perform the computation in a finite domain, boundary conditions must be imposed to avoid the artifacts due to the boundary reflections. Engquist and Majda (1977) proposed absorbing boundary conditions for modeling schemes

based on finite difference of full acoustic equation, Calyton and Engquist (1980) developed absorbing boundary condition for the wave equation migration in two dimensional case. Here we generalize to three dimensional case using the approximation of the square-root operator, i.e. the dispersion relations. Considering the finite-difference migration operator k_{z3} in Eq. (58), i.e.,

$$k_{z3} = \frac{b\frac{v}{\omega}(\frac{\partial^2}{\partial x^2} + \frac{\partial^2}{\partial y^2})}{1 + a\frac{v^2}{\omega^2}(\frac{\partial^2}{\partial x^2} + \frac{\partial^2}{\partial y^2})}. \tag{79}$$

To ensure stability, the second-order derivative $\frac{\partial^2}{\partial x^2}$ or $\frac{\partial^2}{\partial y^2}$ should be avoided at the different sides of the boundary (Clayton and Engquist, 1980). Transforming Eq. (79) into the frequency-wavenumber domain, it can be written as

$$k_{z3} = -\frac{b\frac{v}{\omega}(k_x^2 + k_y^2)}{1 - a\frac{v^2}{\omega^2}(k_x^2 + k_y^2)}. \tag{80}$$

Supposing the computational domain is given by $x_0 \le x \le x_1, y_0 \le y \le y_1$, then the value of k_{z3} at $x = x_0$ is chosen as

$$k_{z3} = -\frac{\alpha\frac{v}{\omega}k_x + b\frac{v}{\omega}k_y^2}{1 - \beta\frac{v^2}{\omega^2}k_x - a\frac{v^2}{\omega^2}k_y^2}, \tag{81}$$

where α and β are determined by matching dispersion relation at the boundary $x = x_0$ to the interior. The differential equation corresponding to Eq. (81) is

$$[1 + i\beta\frac{v^2}{\omega^2}\frac{\partial}{\partial x} + a\frac{v^2}{\omega^2}\frac{\partial^2}{\partial y^2}]\frac{\partial P}{\partial z} = i[i\alpha\frac{v}{\omega}\frac{\partial}{\partial x} + b\frac{v}{\omega}\frac{\partial^2}{\partial y^2}]P. \tag{82}$$

where $i = \sqrt{-1}$. The splitting form is given by

$$\begin{aligned}&[1 + i(\frac{\beta v}{\omega} - i\frac{\Delta z\alpha}{2})\frac{v}{\omega}\frac{\partial}{\partial x}][1 + (\frac{av}{\omega} - i\frac{b\Delta z}{2})\frac{v}{\omega}\frac{\partial^2}{\partial y^2}]P^{n+1}\\ &= [1 + i(\frac{\beta v}{\omega} + i\frac{\Delta z\alpha}{2})\frac{v}{\omega}\frac{\partial}{\partial x}][1 + (\frac{av}{\omega} + i\frac{b\Delta z}{2})\frac{v}{\omega}\frac{\partial^2}{\partial y^2}]P^n.\end{aligned} \tag{83}$$

The finite-difference scheme for Eq. (83) can be expressed as

$$[1 + i\gamma_1\delta_x^0]Q_{k,l}^{n+1} = [1 + i\gamma_2\delta_x^0][1 + \eta_2\delta_y^2]P_{k,l}^n, \tag{84}$$

where

$$\gamma_1 = (\frac{\beta v}{\omega} - i\frac{\alpha\Delta z}{2})\frac{v}{2\omega\Delta x}, \quad \gamma_2 = (\frac{\beta v}{\omega} + i\frac{\alpha\Delta z}{2})\frac{v}{2\omega\Delta x}, \tag{85}$$

$$\eta_1 = (\frac{av}{\omega} - i\frac{b\Delta z}{2})\frac{v}{\omega\Delta y^2}, \quad \eta_2 = (\frac{av}{\omega} + i\frac{b\Delta z}{2})\frac{v}{\omega\Delta y^2}, \tag{86}$$

δ_x^0 and δ_y^2 are the second order central difference operator defined by

$$\delta_x^0 P_{k,l}^n = P_{k+1,l}^n - P_{k-1,l}^n, \quad \delta_y^2 P_{k,l}^n = P_{k,l+1}^n - 2P_{k,l}^n + P_{k,l-1}^n. \tag{87}$$

Q^n in Eq. (84) is the intermediate wavefield and P^{n+1} is computed by the following scheme

$$[1 + \eta_1\delta_y^2]P_{k,l}^{n+1} = Q_{k,l}^{n+1}. \tag{88}$$

For the boundary condition at $x = x_1$, it can be determined by substituting b and α with $-b$ and $-\alpha$ in Eqs. (82) $\sim$ (88). Similarly, the absorbing boundary conditions at $y = y_0$ and $y = y_1$ can be derived, but we will not reported Here,

3. Parallel computations

Parallel computations offer a new powerful technique for large-scale scientific computing, and message passing interface (MPI) is regarded as one of the standard tools for parallel computing. The key issues to guarantee the success of a parallel algorithm are to minimize the communications between the processors and ensuring one task per processor can be implemented independently. Here, the parallel implementation using MPI system for the wavefield extrapolation algorithms presented in the previous section is briefly described.

For the 3D shot-gather migration problem considered in this paper, spatial parallelism rather than the frequency parallelism has a good scalability, so that it can be effectively extended to solver large scale problems. In the spatial parallelism, the entire space domain is split into a set of smaller subdomains. Then, in each subdomain, the wavefield extrapolation for the downgoing wave D and the upgoing wave U is computed directly by one processor and the image of the subdomain is generated separately. The communications between processors are required only at the starting and ending of computations. At the starting, data used for each subdomain is sent to the corresponding processor from the main node, and then each processor carries out its own task independently. After the images of each subdomain are completed, they are forward to the main node and stack together using Eq. (76) to form the entire imaging. One convenient spatial splitting scheme is according to the scope of each shot line. The flow chart of the spatial parallelism is displayed in Fig. 3. The procedure is as follows: enter the MPI system, each processor will receive the corresponding shot-gather data and the velocity data. Then the migration process is performed and yields individual subdomain images. These images are stored on all processors and finally are gathered together to produce the entire images for the main processor. Since the communications are only needed at the starting to send out data and to collect and stack data at the ending, no other message communication is required during the wavefield extrapolation. Hence, an excellent computational efficiency (nearly 99%) is achieved. Other parallel algorithms, such as the frequency parallelism, and the frequency and space simultaneous parallelism can be considered, but they are not discussed in this work.

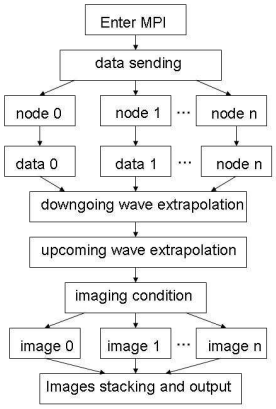

Figure 3. Flow chart parallel computation for 3D shot-gather migration

4. Numerical simulations

To validate and to investigate the effectiveness of the parallel hybrid method for 3D prestck deep imaging, we present two numerical simulations.

The first case study focuses on the SEG/EAEG subsalt model, which has been regarded as a benchmark model to test capability of various migration or inversion algorithms developed for exploration applications. The model has been used to verify other wavefield extrapolation algorithms (Zhang and Zhang, 2004).

For the SEG/EAEG subsalt model, the data is generated from the shot-gather data corresponding to 50 shot lines and each line has 68 by 6 seismic traces. The line space is $160m$ and the shot space is $80m$. The spatial step sizes Δx, Δy and Δz are $40m$, $40m$ and $20m$, respectively. The record length is $4992s$ with $8ms$ sampling time. No pre-processing such as the stacking is performed before the migration. Hence, the resulting image is referred as prestack. In the spatial parallelism, each processor is assigned to process partial or the completed shot line.

We now present a typical slice of the 3D shot-profile imaging. Fig. 4 is a vertical slice of the known 3D velocity model at $x = 5500m$, and Fig. 5 is the migration slice at the same position. In both figures, the x direction is chosen as the inline direction, and the y direction represents the crossline direction. Comparisons between Figs. 4 and 5 show that the images of the subsalt are in good agreement.

With the successful validation of our proposed method applied to the well-known benchmark model, the method is then tested to a wavefield extrapolation problem with real data provided by BGP, which is one of the leading geophysical company under the China National Petroleum Corporation(CNPC). The 3D field data are collected from 15964 shots and using 64080 receivers. The maximal offset is $4769.5m$ and the minimal offset is $270.4m$. The trace space is $50m$ and the trace length is $6s$ with $1ms$ sampling rate ($i.e., \Delta t = 1ms$). The line space is $250m$ with $100m$ shot space, and 96 (16 by 6) receivers are placed at each shot. This data set amounts to 215.5G bytes. This is a typical large-scale 3D prestack imaging problem. Figs. 6 and 7 display two slices of the 3D imaging results for inline No.123 and No.127, respectively. The two lines are $1km$ away as the line step is $250m$. Useful information about the main structures can be extracted from these figures, and it clearly reveals that there is a large incline structure with the middle-sized dipping angle in the left area. Moreover, the dips of the stratum are varying smoothly in other areas. The results of the reconstructed images have been utilized by the engineers and researchers at BGP-CNPC.

5. Conclusions

Three-dimensional prestack depth migration based on the wave equation plays an important role in reconstruction of the seismic subsurface structures imaging. In this paper, we present the hybrid method for 3D shot-gather prestack depth migration. The most attractive feature of the proposed method is that it can be implemented using parallel computations, so that tremendous improvement can be achieved. Moreover, the scalability ensues that the method can be effectively extended to deal with large scale problems. Although there are many possibilities to develop parallel algorithms, we focus on the parallelization of the prestack depth migration at the shot loop in order to minimize the communications between processors and to fully utilize the capability of each processor to attain the maximum enhancement in parallel computations. The developed parallel hybrid method has been tested to the well-know benchmark case - the SEG/EAEG model and also to a 3D wavefield exploration with real data provided by BGP-CNPC. From the

simulation results reported here, not only we can validate the proposed method, but we also conclude that the technique is an effective tool for practical application to 3D prestack depth migration.

Acknowledgements

The first author also thanks Professor G. Zhang and Dr. X. Cui for the computations with the real data.

References

[1] Alexander Mihai Popovici, 1996, Prestack migration by split-step DSR: Geophysics, 61(5), 1412-1416.
[2] Baysal, E. D., Kosloff, D. D., Sherwood, J. W. C., 1983, Reverse time migration: Geophysics, 49(9), 1514-1524.
[3] Biondi, B., Gopal Palacharla, 1996, 3-D prestack migration of common-azimuth data: Geophysics, 61(6), 1822-1832.
[4] Claerbout J. F., 1985, Imaging the earth's interior: Blackwell Scientific Publications, Inc.
[5] Claerbout J. F., 1971, Toward a unified theory of reflector mapping: Geophysics, 36(3), 467-481.
[6] Clayton R. W. and Engquist B., 1980, Absorbing boundary conditions for wave-equation migration: Geophysics, 45(5), 895-904.
[7] Collina, F., Joly, P., 1995, Splitting of operators, alternated directions, and paraxial approximations for the three-dimensional wave equation: SIAM J. Sci. Comput., 16, 1019-1048.
[8] Engquist B. and Majda A., 1977, Absorbing boundary conditions for the numerical simulation of waves: Math. Comp., v.31, 629-651.
[9] Gazdag, J., 1978, Wave equation migration with the phase method: Geophysics, 43(1),176-185.
[10] Gazdag, J., Sguazzero, P., 1984, Migration for seismic data by phase shift plus interpolation: Geophysics, 49(1), 124-131.
[11] Hale, D., 1999, Stable explicit depth extrapolation of seismic wave fields: Geophysics, 56(6), 1770-1777.
[12] Louis A. Romero, Dennis C. Ghiglia, Curtis C. Ober and Scott A. Mortor., 2000, Phase encoding of shot records in prestack migration: Geophysics, 65(2), 426-436.
[13] Ottolini, R., Claerbout, J. F., 1984, The migration of common midpoint slant stack: Geophysics, 49, 237-249.
[14] Ristow, D., Rühl, T., 1995, Fourier finite-difference migration: Geophysics, 59(2), 1882-1893.
[15] Ristow, D. and Ruhl, T., 1997, 3-D implicit finite-difference migration by multiway splitting: Geophysics, 62(2), 554-567.
[16] Rietveld, W. E. A., Berkhout, A. J., 1994, Prestack depth migration by means of controlled illumination: Geophysics, 59(5), 801-809.
[17] Schneider, W. A., 1978, Integral formulation for migration in two and three dimensions: Geophysics, 43(1), 49-76.
[18] Stoffa, P. L., Forkema, J. T., de Luna Freire, et al., 1990, Split-step Fourier migration: Geophysics, 55(4), 410-421.
[19] Stolt, R. H., 1978, Migration by Fourier transform: Geophysics, 43(1), 23-38.
[20] Thomas, J. W., 1995, Numericla practical differential equations: finite difference methods. Springer-Verlag, New York.
[21] Zhang, G., Zhang, W., 2004, Methods and numerical experiments for wave equation prestack depth migration: Science in China Series A-Mathematics, Supp. Vol.47.
[22] Zhang, W., 2004, 3-D prestack depth migration with planewave synthesizing method. 74th Ann. Internat. Mtg., Soc. Expl. Geophys., Expanded Abstracts, 10-15 October, Denver, USA.
[23] Zhang, W., Zhang, G., 2005, 3D prestack depth migration with factorization four-way splitting scheme: International Journal of Numerical Analysis and Modeling, Vol.2, Supp. 183-196.
[24] Zhang, W., Zhang, G., 2006, 3D prestack depth migration by hybrid. Expanded Abstracts: SPMI5. SEG International Exposition and Seventy-Sixth Annual Meeting. 2006, 1-6 October, New Orleans, Louisiana,USA.
[25] Zhang, W., Zhang, G., 2006, 3D hybrid depth migration and four-way splitting schemes: Journal of Computational Mathematics, 24(4), 463-474.

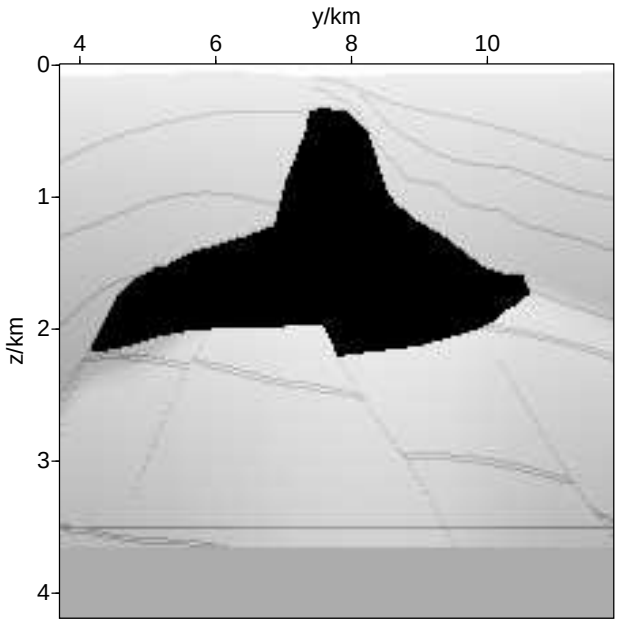

Figure 4. Typical slice of 3D SEG/EAEG salt velocity model at $x = 5500m$.

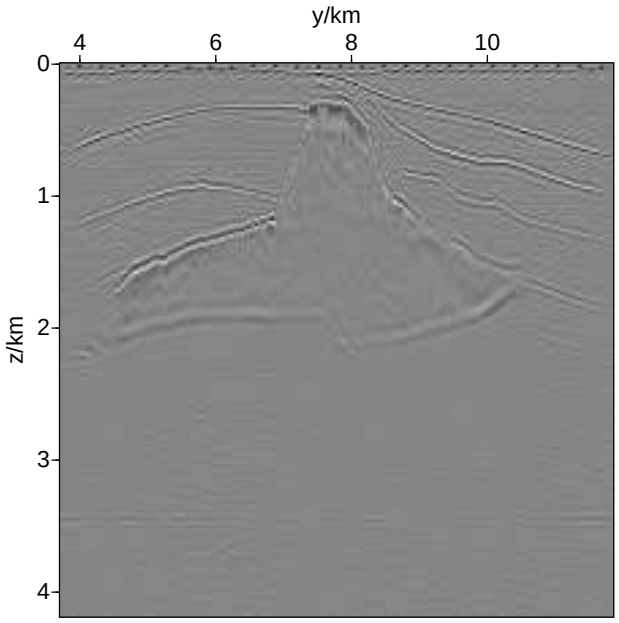

Figure 5. Resulting 3D wave equation imaging at the same position as in Fig. 4.

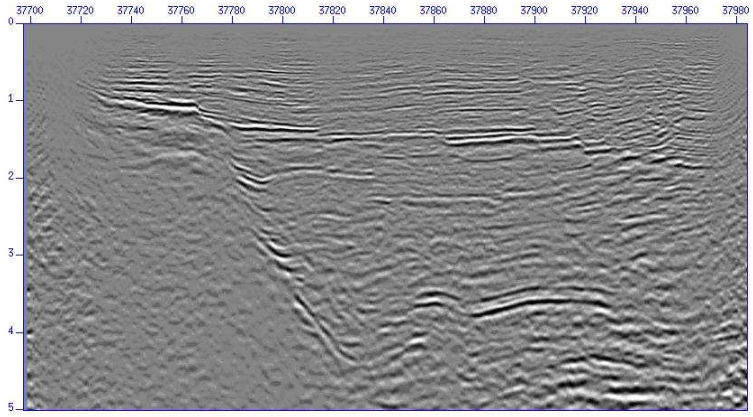

Figure 6. Resulting 3D wave equation imaging for inline No.123.

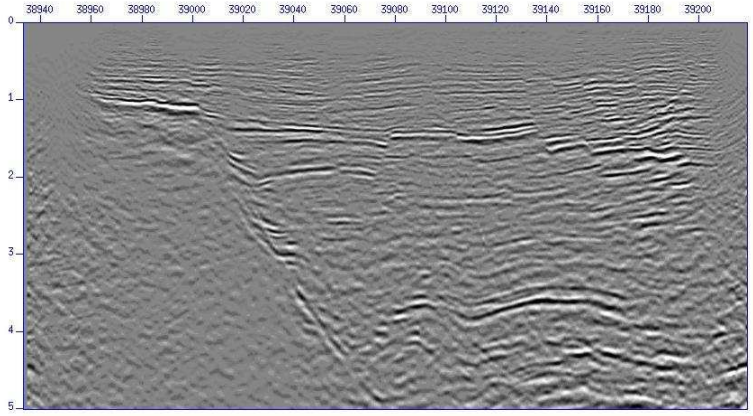

Figure 7. Resulting 3D wave equation imaging for inline No.127.

Institute of Computational Mathematics and Scientific/Engineering Computing, State Key Laboratory of Scientific and Engineering Computing, Academy of Mathematics and Systems Science, Chinese Academy Sciences, Beijing P.O.Box 2719, Beijing 100190, P. R. China
E-mail: Email: zws@lsec.cc.ac.cn

Department of Mathematics and Statistical Sciences, University of Alberta, Edmonton, Alberta, Canada, T6G 2G1
E-mail: Email: yaushu.wong@ualberta.ca